

Functional Defective Metal-Organic Coordinated Network of Mesostructured Nanoframes for Enhanced Electrocatalysis

Gamze Yilmaz, Chuan Fu Tan, Minghui Hong, and Ghim Wei Ho*

Although defects are traditionally perceived as undesired feature, the prevalence of tenacious low-coordinated defects can instead give rise to desirable functionalities. Here, a spontaneous etching of mesostructured crystal, cyanide-bridged cobalt-iron (CN-CoFe) organometallic hybrid into atomically crafted open framework that is populated with erosion-tolerant high surface energy defects is presented. Unprecedentedly, the distinct mechanistic etching pathway dictated by the mesostructured assembly, bulk defects, and strong intercoordinated cyanide-bridged hybrid mediates not only formation of excess low-coordinated defects but also more importantly stabilizes them against prevailing dissolution and migration issues. Clearly, the heteropoly-nuclear cyanide bonded inorganic mesostructured clusters sanction the restructuring of a new breed of stable organometallic polymorph with 3D accessible structure enclosed by electrochemical active atomic stepped edges and high index facets. The exceptional electrocatalysis performance supports the assertion that defective mesostructured polymorph offers a new material paradigm to synthetically tailor the elementary building block constituents toward functional materials.

1. Introduction

Control of structure at the atomic level can effectively tune electro- and heterocatalysis performance, enabling enhancement in both activity and durability. Open polymorphs, specifically nanoframes, have gained extensive attention in recent decades for catalysis, owing to their distinctive 3D open structures endow with cavities at the interior and side faces of a crystal with readily accessible surface sites.^[1] The nanoframes are structurally different from conventional nanoparticulate system. In the latter material system, the high surface-area-to-volume ratio is achieved by isotropically decreasing the overall particle size at the expense

of materials stability. Nanoframes, on the other hand, are structurally more stable since the starting crystal dimensions are preserved, while the interior and side materials are evacuated. This strategy raises the specific surface area and grants optimal 3D molecular accessibility without compromising structural stability. Already, there are a few template-based etching and/or replacement reactions methods that have been reported to successfully prepare open polymorph structures.^[2] Nonetheless, selective and controllable removal of side faces of a nanocrystal with the preservation of its overall frame structure remains particularly challenging, stemming from the difficulty in identifying etchant with appropriate and controllable attrition capabilities.


Other than establishing open polymorphs structure, defect engineering is another effective approach to improve catalytic reactivity through increased density of accessible edges sites.^[3] Moreover,

defects are known to perturb the local density of states and introduce additional energy levels between the valence and conduction bands.^[4] Commonly, defects transpire as low-coordinated atoms (e.g., steps, edges, kinks, etc.) on the surface of the nanocrystals. However, such defects that are derived from classical thermodynamically favorable crystal growth method generally diffuse quickly to adopt minimal total energy which often leads to their disappearances on the eventual nanocrystals surfaces. Another type of defect in a form of quasiperiodic structure or crystal boundaries that occur as polycrystalline or amorphous phase is known to expose many active unsaturated atoms. The amorphous unsaturated atoms not only display strong binding with hydrogen ions in aqueous solution but also expose large fraction of reactive crystal boundaries edge sites. Though nanocrystals that possess amorphous phase have efficient electrocatalytic properties, they are often impaired by high solubility and low stability in aqueous electrolyte issues.

Herein, we explicitly exploited nonclassical crystallization pathway via colloidal intermediates and mesoscale transformation^[5] to form crystalline structures of nanoscopic building units that show translational ordering into a mesostructured Prussian blue analogues (PBAs) crystal. The mesostructured crystals are devised to comprise of synergistic organometallic hybrid, i.e., inorganic superstructures with atomically coordinated organic cyanide (CN) bridge. Leveraging on the hybrid mesostructured

Dr. G. Yilmaz, C. F. Tan, Prof. M. Hong, Prof. G. W. Ho
Department of Electrical and Computer Engineering
National University of Singapore
4 Engineering Drive 3, Singapore 117583, Singapore
E-mail: elehwg@nus.edu.sg

Prof. G. W. Ho
Institute of Materials Research and Engineering
A*STAR (Agency for Science, Technology and Research)
3 Research Link, Singapore 117602, Singapore

 The ORCID identification number(s) for the author(s) of this article can be found under <https://doi.org/10.1002/adfm.201704177>.

DOI: 10.1002/adfm.201704177

crystal constitution, we report selective chemical etching that leads not only to otherwise unexposed and unstable high indexes facets but also complex polymorphs morphologies. More importantly, we highlight the premise of mesostructural building blocks, bulk defects, and cyanide molecular bridges that resist the erosion/migration of low-coordinated highly reactive excess stepped edges. This is contrary to the classical ionic/molecular crystallization that evolves crystal nuclei that are adversely prone to high solubility and diffusion limitations, whereby low-coordinated atoms are susceptible eroded. To this end, judicious design of 3D molecular accessibility nanoframes with hollow interior, crafted side faces, and engineered defects that manifest as stable low-coordinated atoms and amorphous edge terminated structures have been realized. The proof-of-concept electrochemical demonstrations attest the remarkable catalytic activity, reaction kinetics, and stability of the hybrid nanoframes. The exceptionally active and stable nanoframes, bearing defective yet functional low-coordinated defects with the amelioration of the structural fragilities issue, capitalize on the mesoscale assemblies and strong intercoordination of metal ions–organic linker. Finally, the mesostructured crystal can be

recognized as a new breed of heterogeneous electrochemical active materials with boundless opportunities to synthetically tailor its atomic bonding and crystal structure through the mesoscale structure in tandem with composition, well-beyond the conventional material system.

2. Results and Discussion

PBAs surrounded with redox-active transition metal ions are employed for the synthesis of the CoFe-PBA nanocubes (CF-NCs). The coordination compounds of PBAs are described by $A_xM'[M''(CN)_6]_y \cdot \Theta_{1-y} \cdot nH_2O$, where M' and M'' are transition metals coordinated with carbon and nitrogen, A is alkaline cation and Θ is $M''(CN)_6$ vacancy; $0 < x \leq 2$ and $0 < y \leq 1$.^[6] The well-defined organometallic CF-NCs are synthesized through a room temperature kinetically controlled crystallization of potassium ferricyanide and cobalt ions (Figure 1a).^[7] Chemical etching of CF-NCs into CoFe-PBA octopod nanoframes (CF-ONFs) with eight arms extending from the center toward the corners of the cube framework is illustrated in Figure 1b.

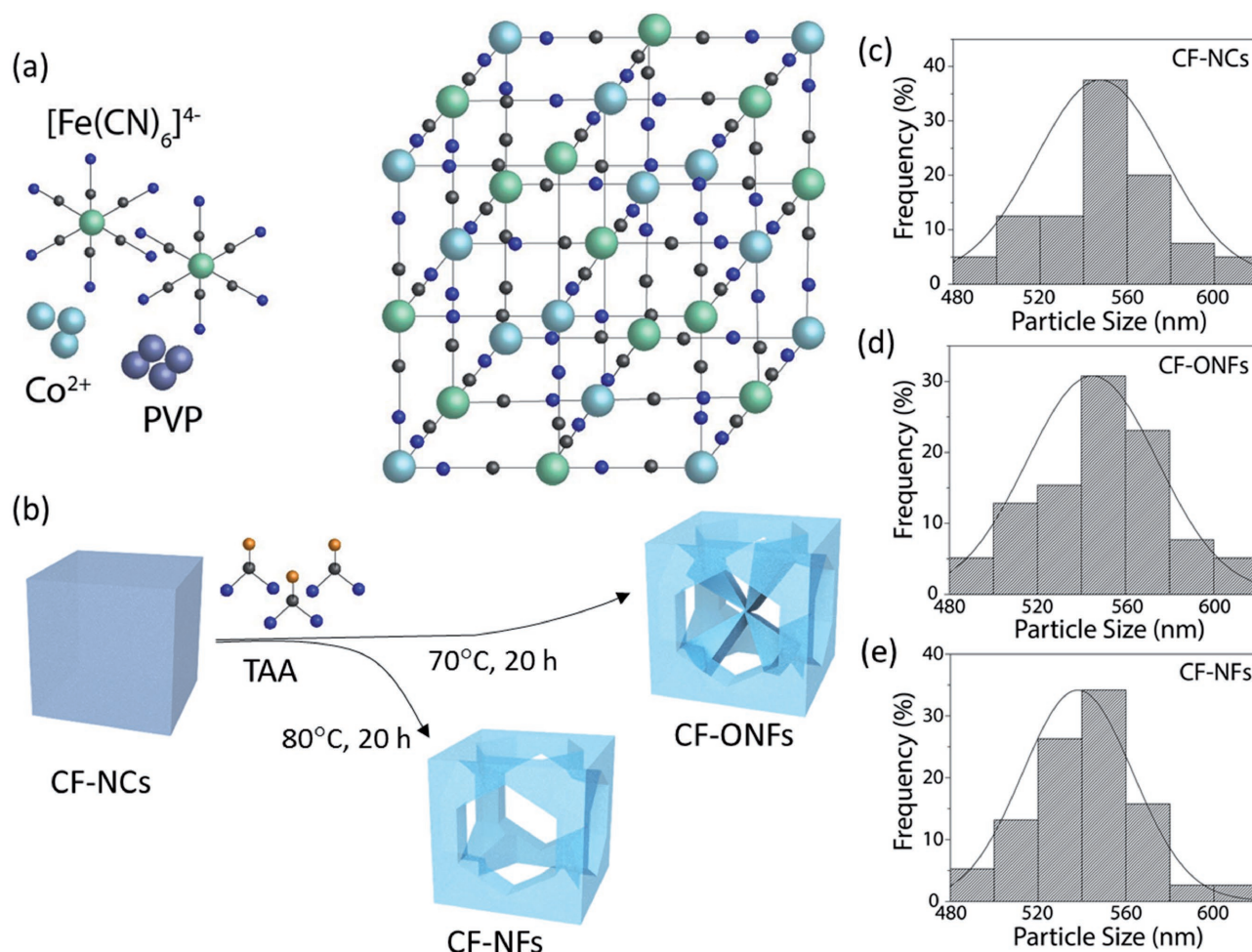


Figure 1. a) Representation of CoFe-PBA network. (Co, blue; Fe, green; C, gray; N, dark blue; alkaline ions and H_2O were not presented for clarity.) b) Schematic illustrations for the formation of CoFe-PBA octopod nanoframes (CF-ONFs) and nanoframes (CF-NFs) (S, yellow). Particle size distribution histograms of c) CF-NCs, d) CF-ONFs, and e) CF-NFs.

While CoFe-PBA nanoframes (CF-NFs) with only trusses and open side faces are synthesized at similar conditions except at a higher thioacetamide (TAA) etching of 80 °C (Figure 1b). The initial solid PBA nanocubes are evolved into 3D accessible surfaces of high surface-to-volume ratio and high atomic utilization polymorphs. Similar size distributions of CF-NFs, CF-ONFs, and CF-NFs (Figure 1c–e) suggest preferential interior etching process. The end-product of the as-synthesized CF-NFs, CF-ONFs, and CF-ONFs powder is shown in Figure S1 (Supporting Information).

The panoramic scanning electron microscopy (SEM) images of the as-synthesized CF-NFs, CF-ONFs, and CF-NFs are shown in Figures S2–S4 (Supporting Information). In detail,

the as-synthesized CF-NFs show uniform solid nanocubes with an average edge length of 550 nm (Figure 2a). Careful SEM observations of the CF-NFs reveal nanoscopic roughness on the surface and edges of the nanocubes^[8] which corroborate the transmission electron microscopy (TEM) analyses (Figure 2d). Figure 2b,e shows the respective SEM and TEM images of CoFe-ONFs consisting of eight arms protruding from the center to the corners of the nanoframe. Broken CoFe-ONFs reveal symmetrical arms of average length ≈ 200 nm (Figure S5, Supporting Information). On the other hand, CF-NFs exhibit only nanocube skeletal framework without any supporting core (Figure 2c,f). Notably, the overall size and structural framework of the CF-NFs are well-preserved, while the interior and

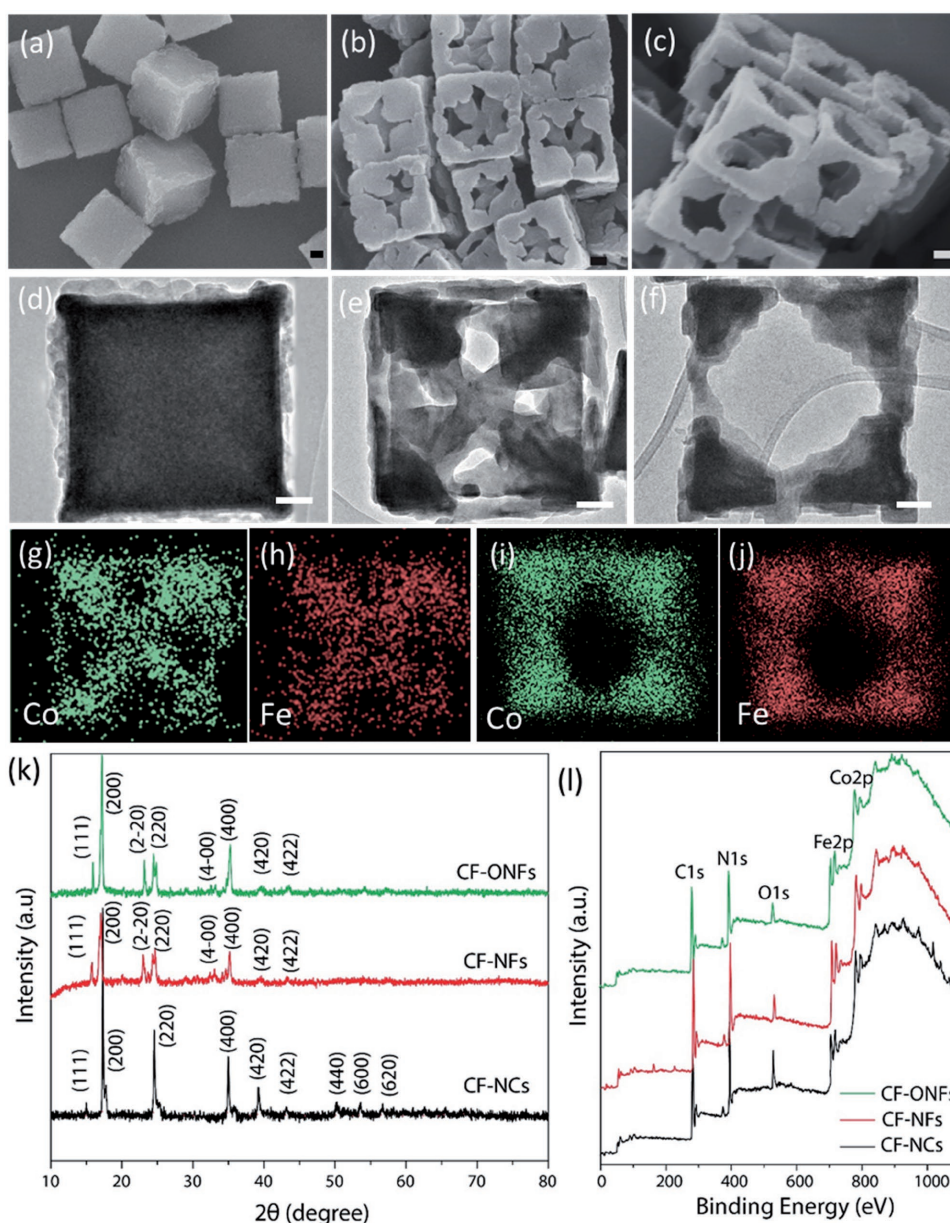


Figure 2. SEM images of a) CF-NFs, b) CF-ONFs, and c) CF-NFs. Low-resolution TEM images of d) CF-NFs, e) CF-ONFs, and f) CF-NFs. The scale bar is 100 nm. EDX elemental mapping images of g,h) CF-ONFs and i,j) CF-NFs for Co (blue) and Fe (orange). k) XRD patterns and l) XPS survey spectrum of CF-NFs, CF-ONFs, and CF-NFs.

side faces are selectively etched. Moreover, abundant stepped surfaces throughout the edges are evidently seen throughout the surfaces of CF-NFs (Figure 2f). Energy dispersive X-ray (EDX) elemental mapping images of the CF-NC (Figure S6, Supporting Information), CF-ONF (Figure 2g,h), and CF-NF (Figure 2i,j) show uniform distributions of the Fe and Co elements throughout the structures. Meanwhile, the Co: Fe: K atomic ratios of all the specimens are determined using TEM-EDX and inductively coupled plasma optical emission spectroscopy (ICP-OES) (Table S1, Supporting Information). The CF-NFs have higher Co: Fe: K ratio compared with the CF-NCs and CF-ONFs, indicating substantial loss of interstitial K ions during etching. Based on the ICP elemental analysis, the CF-NCs, CF-NFs, and CF-ONFs can be described by chemical formulas of $K_{0.22}Co[Fe(CN)_6]_{0.69}$, $K_{0.16}Co[Fe(CN)_6]_{0.76}$, and $K_{0.27}Co[Fe(CN)_6]_{0.88}$, respectively. Figure S7a–c (Supporting Information) shows the interior, nonetched parts of the CF-NC, CF-NF, and CF-ONF, respectively. The lattice fringes show interplanar spacing of 0.520 nm that is assigned to the (200) plane of the CoFe-PBAs. The CF-NFs and CF-ONFs also indicate the existence of the (220) CoFe-PBAs with interlayer spacing of 0.366 nm. CF-NCs show X-ray diffraction (XRD) pattern that can be indexed to face-centered-cubic (fcc) structure of a typical cobalt–iron Prussian blue analogue with a unit cell parameter of $a = 10.18 \text{ \AA}$ (Figure 2k).^[7,9] After the etching process, the fcc crystal symmetry of the original solid nanocubes are distorted and structurally transformed into rhombohedral hollow CF-ONFs and CF-NFs (Figure 2k and Figures S8–S11, Supporting Information).^[7] The presence of Co, Fe, O, C, and

N elements after etching of the as-synthesized CF-NFs and CF-ONFs is shown by X-ray photoelectron spectroscopy (XPS) survey scan (Figure 2l). As can be seen, the absence of sulfur peak suggests the exclusive etchant functionality of TAA and the purity of CF-NFs and CF-ONFs. Moreover, the role of TAA as the etchant is further verified (Figures S12–S14, Supporting Information).

Based on the time-dependent evolution studies (Figures S15 and S16, Supporting Information), a plausible mesostructures defect mediated etching process is proposed. As previously reported, the mesocrystalline features of PBAs can be formed by a nonclassical crystallization process.^[10] To verify the proposed etching mechanism, contrasting solid NiFe-PBA nanocubes (NF-NCs) of smooth surfaces, mostly defect-free edges and high crystallinity, were synthesized (Figures S17–S19, Supporting Information). When the same etching route of CF-NFs is applied to the dense and compact NiFe-PBA nanocubes, irregular and minimally etched polymorphs are mostly formed instead (Figure S20, Supporting Information). To further elucidate the mesostructured crystal features of CF-NCs, complementary surface topography and porosity characterizations are performed. Figure 3a shows the SEM image of CF-NCs where multitude clustering of subunits elementary building blocks (indicated by arrows) are observed. Atomic force microscopy (AFM) image and the corresponding height profile of the CF-NCs (Figure 3b) further substantiate the presence of rough surfaces, contrary to the solid NF-NCs which present smooth and flat surfaces (Figure S21, Supporting Information). Moreover, as determined by the nitrogen (N_2)

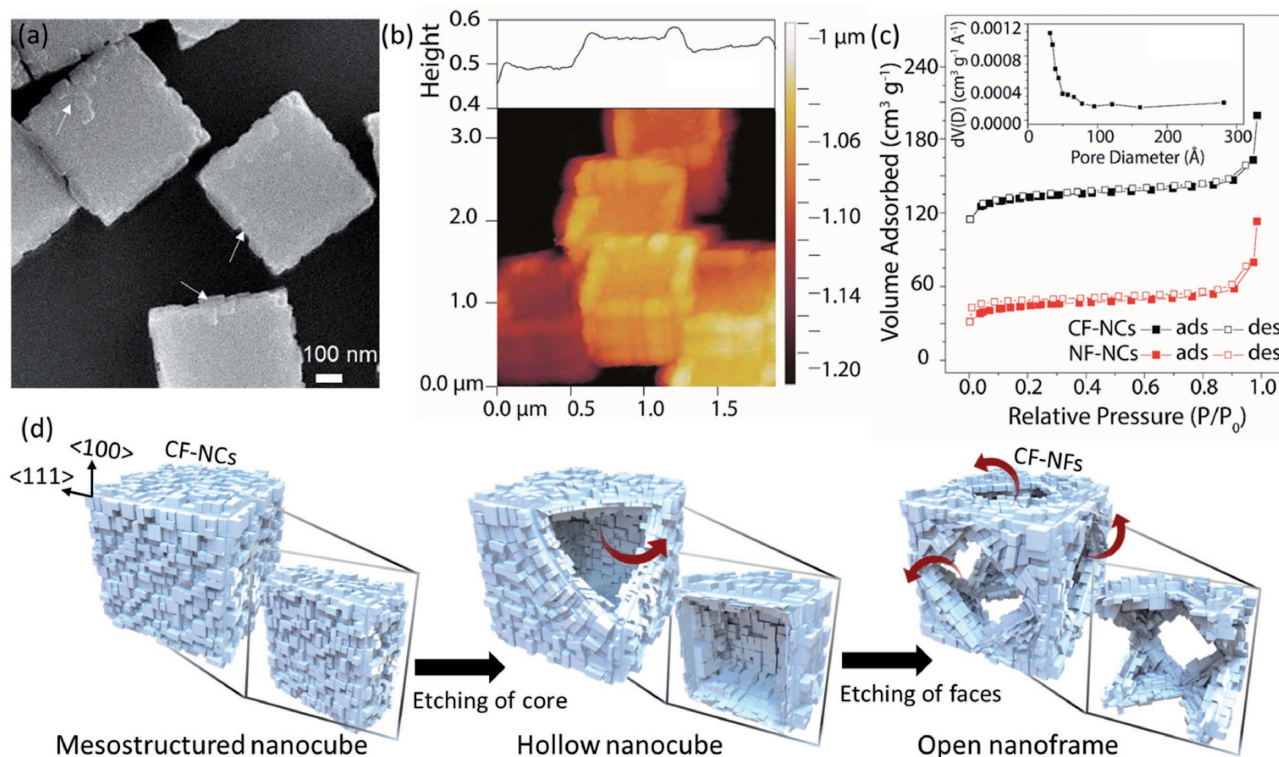


Figure 3. a) SEM and b) AFM images of CF-NCs with the corresponding height profile. c) N_2 adsorption and desorption isotherms of CF-NCs and NF-NCs. Inset: Pore size distribution of CF-NCs. d) Schematic illustration of the formation process of CF-NFs from CF-NCs.

sorption measurements (Figure 3c and inset), CF-NCs exhibit a high surface area of $339.3 \text{ m}^2 \text{ g}^{-1}$ (as opposed to NF-NCs of $139.6 \text{ m}^2 \text{ g}^{-1}$) with a mesoporous structure dominated by a narrow pore size distribution of $\approx 3 \text{ nm}$. The notable presence of undulated surfaces, high density narrow pores accompanied by considerable internal porosity corroborates mesocrystal constitution of CF-NCs. During the nonclassical crystallization of mesostructured crystals, abundant defects are introduced in the framework, specifically throughout the interior core of the cubic PBAs.^[8,11] The density and distribution of the defects cause site-selective instabilities and thus determine the course of etching kinetics.^[7] As schematically illustrated in Figure 3d and supported by the time evolution synthesis studies (Figure S15, Supporting Information), the CF-NFs are

formed by successive core followed by face etching processes. The intrinsic self-assembled subunits of building blocks allow readily customization of mesostructured nanocube into open nanoframe that is enclosed by extensive stepped surfaces with low-coordinated atomic surfaces.

Modifying the structure and composition of nanocrystals is a powerful strategy to tailor the chemical and physical properties of the materials.^[12] Nanocrystals modified via chemical etching can take the advantage of emergence of novel architectures with etched surfaces enclosed by high-index facets.^[13] While high-index facets, which are composed of low coordinated atoms, are expected to exhibit low stability due to high surface energies that generally vanish during crystal growth, they can be effectively generated by etching, and stabilized by a large number of

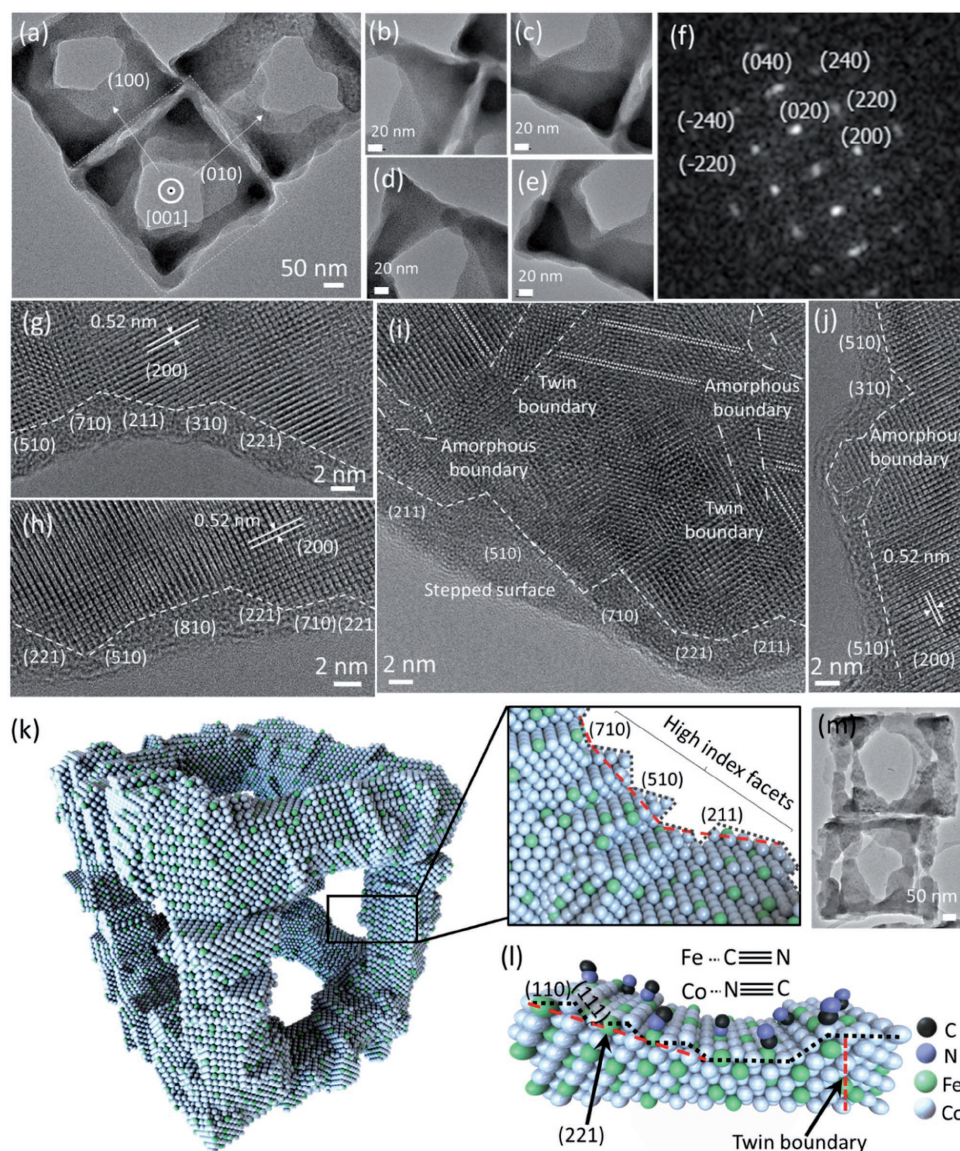


Figure 4. a) TEM image for the nanoframes and b–e) enlarged regional TEM examination for the etched edges. f) The SAED pattern along [001] direction. g, h) High-resolution TEM images of the etched edges of the nanoframes showing the stepped high-index facets. i, j) Atomic resolution images of the etched edges of the nanoframes showing the defect-rich surfaces. k, l) Atomic model of high index facets and low coordinated defects of m) CF-NFs (TEM image).

atomic steps and bulk defects as well as the strong interatomic framework.^[3b,14] Figure 4a–e shows the low-resolution TEM images of CF-NFs and corresponding individual four corners of the inner etched nanoframes regions. The high-resolution TEM imaging of the nanoframes is projected from [001] direction. The selected area electron diffraction (SAED) pattern (Figure 4f) shows diffraction pattern with elongated spots that indicates single-crystal-like mesostructure. Figure 4g,h shows lattice fringes of 0.520 nm interplanar spacing, which can be assigned to (200) planes of the CF-NFs. The Miller indices of the exposed facets surrounding the etched surfaces can be specified by measuring the interfacial angle enclosed by (200) plane and the facet of interest (Table S2, Supporting Information). As can be seen from Figure 4g,h and Figures S22–S25 (Supporting Information), the etched surfaces are enveloped by various high-index facets, including (310), (510), (710), (810), (221), and (211) facets, with a high density of atomic steps. The most predominant facet found on the nanoframes is (221) which is composed of energetically favorable (110) atomic steps and (111) atomic terraces (Figure 4l and Figure S26, Supporting Information). Similar to the stabilizing effect of the atomic steps of high-index facets, bulk defects (twining boundaries, amorphous boundaries, and stacking faults) have also been suggested to induce stabilization of the surface atomic steps.^[3b,14a–c] Figure 4i,j and Figure S27 (Supporting Information) show various bulk defects identified throughout the surface, indicating the defect-rich CF-NFs. Amorphous regions surrounded by crystalline matrix are observed as well as twin boundaries are identified at the locations where the continuous lattice fringes terminate and change direction. Furthermore, chemical integrity and stability of PBAs are maintained by tight bonding between cyanide ligand and transition metal ions through $d\pi-p\pi$ interactions.^[15] The heteropolynuclear cyanide complex, CoFe-PBA is also exploited to stabilize low-coordinated defects by means of high electronegativity and substantial σ -bonding of cyanide that can adequately stabilize diverse stereochemical configurations and metal oxidation states.^[15] Hence, the distinctive bulk defects and strong intercoordinated cyanide-bridged hybrid mediates not only formation of excess low-coordinated defects but also intrinsically stabilizes them against prevailing migration and dissolution challenges as presented in Figure 4k–m.

It has been proposed that surface defects including atomic height steps, kinks in steps, twin boundaries, and amorphous boundaries can modify the local electronic structure, inducing high catalytic activity toward molecular adsorption and breakage of the chemical bonds.^[3b,14,16] Consequently, a proof-of-concept electrocatalysis is demonstrated to verify the stability and reactivity of the defective organometallic hybrids toward hydrogen evolution reaction (HER) and oxygen evolution reaction (OER) in 1 M KOH. The representative linear sweep voltammetry (LSV) polarization curves of the potential catalysts are shown in Figure 5a. The swift cathodic current density responses of CF-NFs and CF-ONFs to the applied negative potential indicate superior catalytic activities of the catalysts compared to CF-NCs that exhibit inferior HER activity with a larger onset potential. In contrast, CF-NFs and CF-ONFs exhibit much lower onset potentials under alkaline conditions, which is highly desirable since most of the best reported HER catalysts work under acidic conditions, poses

a challenge to the commercialization of traditional alkaline water electrolysis technologies. To deliver a current density of 10 mA cm^{-2} , CF-NFs and CF-ONFs require overpotentials of 78.1 and 82.6 mV, respectively. These overpotentials surpass most of the reported values obtained using noble-metal-free HER catalyst under acidic and alkaline conditions (Table S3, Supporting Information). To investigate the HER kinetics of the electrocatalysts, the Tafel slopes using the polarization curves are determined (Figure 5b). Tafel slopes of ≈ 39.3 , 45.2, and 59.9 mV decade⁻¹ are obtained for CF-NCs, CF-ONFs, and CF-NCs, respectively. Essentially, the catalytic activity of the CF-NCs is significantly enhanced by structural transformation of nanocubes into nanoframes (CF-NFs) via etching of intrinsically mesostructured PBA crystals into abundant stepped surfaces. The excellent HER catalytic activity of the CF-NFs arises from the highly reactive high-index facets and defect-rich structure consisting of redox-active materials (Co, Fe). Moreover, the bimetallic CoFe constituents of the CF-NFs can synergistically optimize hydrogen adsorption energy and kinetic energy barrier for H–H formation as suggested by previous works on bimetallic nanocrystals.^[17] Importantly, zeolite-like open metal-organic framework of CoFe-PBAs provides highly accessible diffusion pathways for facile electrolyte transportation and permeation, which is believed to be responsible for fast HER kinetics.^[8] It is noted that NiFe-PBAs with truncated corners nanocube and hollow structure (NF-TCs) prepared by etching of NF-NCs under strong alkaline conditions (Figures S28–S30, Supporting Information) show lower electrocatalytic performance (Figure S31, Supporting Information) than CoFe polymorphs.

The superior electrode kinetics of CoFe-PBAs and its derivatives were studied by electrochemical impedance spectroscopy (EIS) and electrochemically active surface area (ECSA) measurements. EIS results depicted in Figure 5c show that, compared to CF-NCs and CF-ONFs, CF-NFs exhibits smaller solution resistance (R_s) and charge transfer resistance (R_{ct}) at high frequency range and steeper straight line along the imaginary axis at low frequency range, indicating lower diffusion resistance. Moreover, ECSA measurements were performed by analyzing the cycling voltammograms at different scan rates between 0.1 and 0.3 V where no redox peaks appear (Figure 5d,e and Figure S32, Supporting Information). The capacitances of 42.6, 37.3, and 26.7 mF cm⁻² were calculated for CF-NFs, CF-ONFs, and CF-NCs, respectively. Higher capacitive performance of CF-NFs is an evidence of the rich electroactive sites in the structure. Besides the good performance of electrocatalysts determined by LSV measurements and supported by cyclic voltammetry and EIS analyses, another important factor in assessing the electrocatalytic activity is the durability of the catalysts over long-lasting continuous electrolysis. This was assessed by 80 h of continuous operation under a constant current density of -25 mA cm^{-2} (Figure 5f). Notably, CF-NCs, CF-NFs, and CF-ONFs exhibited exceptional stability with small degradation after successive 80 h of HER (Figure S33, Supporting Information). The field emission-scanning electron microscopy (FESEM) images of CF-NFs, CF-ONFs, and CF-NCs show structural preservation of all the specimens after prolong electrocatalysis testings (Figure S34, Supporting Information). The TEM images of CF-NFs taken

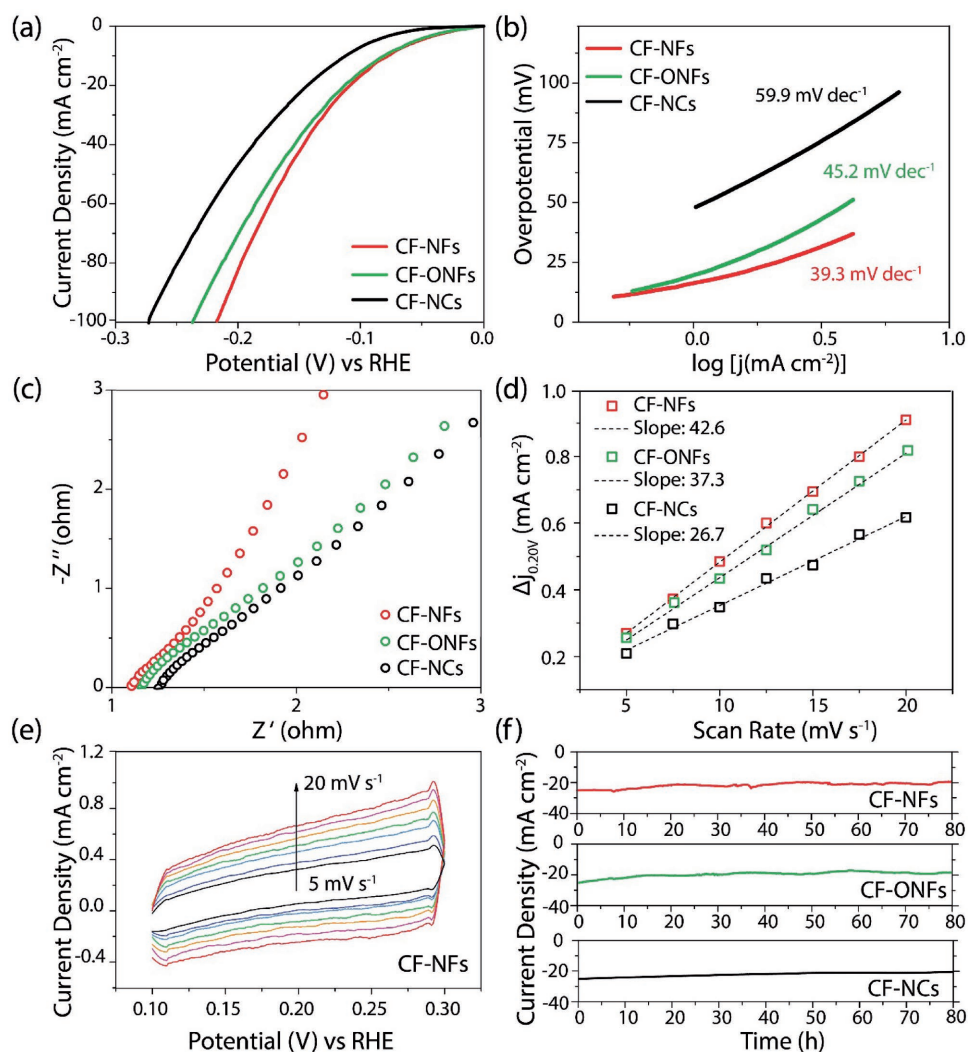


Figure 5. a) Polarization curves of CF-NF, CF-ONF, CF-NC, NF-TCs, and NF-NCs measured at 5 mV s^{-1} in 1 M KOH . b) Corresponding Tafel slopes for the electrocatalysts presented in (a). c) Electrochemical impedance measurements and d) electrochemical active surface area measurements for CF-NF, CF-ONF, and CF-NC. e) Cyclic voltammograms for CF-NF recorded at $5, 7.5, 10, 12.5, 15, 17.5,$ and 20 mV s^{-1} within a potential range of $0.1\text{--}0.3 \text{ V}$ using 1 M KOH . f) Chronoamperometry tests for CF-NF, CF-ONF, and CF-NC.

after stability test are shown in Figure S35 (Supporting Information). At higher magnifications (Figure S36, Supporting Information), it is evident that the CF-NFs are structurally stable, capable of preserving substantial high-index facets after long electrolysis operation, suggesting effectiveness of intercoordination of metal ions–cyanide interactions and bulk defects in stabilizing the atomic steps. Moreover, considering the promising OER performance of the Co, Ni, and Fe containing oxides,^[18] as-synthesized samples were annealed under oxygen environment (see the Experimental Section, and Figures S37 and S38 in the Supporting Information) and evaluated as OER electrocatalysts (Figures S39 and S40, Supporting Information). Among all the tested specimens, CF-NFs-O exhibits the lowest Tafel slope of $65.7 \text{ mV decade}^{-1}$ with a respectable overpotential of 340 mV at 10 mA cm^{-2} (Table S4, Supporting Information), demonstrating attractive OER functionalities through facile oxidation process.

3. Conclusion

We report here the synthesis of cyanide-bridged cobalt–iron (CN-CoFe) organometallic hybrid with atomically crafted open framework. The emergence of novel architecture 3D molecular accessible structures enclosed by abundant atomic stepped edges and high index facets is shown to be the result of direct etching of the mesostructured organometallic PBA. On the contrary to the classical ionic/molecular crystallization, crystals formed via nonclassical crystallization are insusceptible to ionic solubility and migration issues that often limit materials applications. The findings reveal the significance of tenacious yet functional surface and bulk defects that capitalize on the mesoscale assemblies and strong intercoordinated metal ions–organic linker. The nanoframes display exceptional electrochemical performance for bifunctional OER and HER along with high stabilities. The open polymorphs provide a good

platform for the design of multiconstituents atomic structures, potentially beneficial for diverse energy conversion and storage applications.

4. Experimental Section

Synthesis of M-Fe (M = Co and Ni) Prussian Blue Analogue Nanocubes (CF-NCs and NF-NCs): 0.175 g of $\text{Co}(\text{NO}_3)_2 \cdot 6\text{H}_2\text{O}$ or $\text{Ni}(\text{NO}_3)_2 \cdot 6\text{H}_2\text{O}$ was dissolved in 30 mL DI water. Then, 0.25 g sodium citrate and 0.3 g of polyvinylpyrrolidone (PVP) (K30) were added into the solution and stirred for 30 min to form Solution A. Afterward, in a separate container, 0.1 g of $\text{K}_3[\text{Fe}(\text{CN})_6]$ was dissolved in 20 mL DI water to prepare Solution B. Solution B was added into Solution A, stirred for 5 min, and aged for precipitation for 24 h. Brown (CF-NCs) and yellow (NF-NCs) products were collected by centrifugation, washed with ethanol and DI water in sequence for at least two times, and dried in an oven at 60 °C for 12 h.

Synthesis of CF-NFs and CF-ONFs: Typically, 75 mg of CoFe-PBAs and 100 mg of TAA were dissolved in 20 mL DI water and kept at 80 °C and 70 °C for 20 h to obtain CF-NFs and CF-ONFs, respectively. The green colored products were centrifuged, washed with ethanol for several times, and dried in an oven at 60 °C for 12 h.

Synthesis of NF-TCs: 40 mg of NiFe-PBAs and 100 mg of TAA were dissolved in 20 mL DI water. Then, 0.35 mL ammonia was added into the former solution and stirred for a few minutes. The obtained mixture was kept for 12 h at 80 °C. The green colored product was centrifuged, washed with ethanol for several times, and dried in an oven at 60 °C for 12 h.

Synthesis of CF-NFs-O, CF-ONFs-O, CF-NCs-O, NF-TCs-O, and NF-NCs-O: The as-synthesized CoFe-PBA nanoframes, CoFe-PBA octopod nanoframes, CoFe-PBA nanocubes, NiFe-PBA truncated nanocubes, and NiFe-PBA nanocubes were annealed under air for 2 h at 350 °C to obtain CF-NFs-O, CF-ONFs-O, CF-NCs-O, NF-TCs-O, and NF-NCs-O, respectively.

Characterization: FESEM was performed on a JEOL FEG JSM-7001F, equipped with an Oxford/INCA EDX, to study the morphology of the materials. TEM and high-resolution transmission electron microscopic images were recorded by an FEI Tecnai F20 X-TWIN microscope at an acceleration voltage of 200 kV. The elemental mapping of the materials was performed by EDX spectroscopy attached to the JEOL JEM-2010 F TEM instrument. The crystal structure was obtained by X-ray diffraction (XRD) by collecting the patterns using a diffractometer (GADDS XRD system, Bruker AXS) equipped with a Cu $\text{K}\alpha$ radiation source ($\lambda = 1.54 \text{ \AA}$). XPS measurements were performed on a PHI Quantera x-ray photoelectron spectrometer with a monochromated Al $\text{K}\alpha$ radiation. ICP analysis was conducted on dual-view Optima 5300 DV ICP-OES to measure the elemental compositions. Nitrogen adsorption-desorption isotherms were obtained at 77.3 K using the (Quantachrome) NOVA-1200 System and pore size distribution was calculated by BJH method based on desorption isotherm. The surface topography was investigated by AFM using Park-Systems-NX20.

Electrode Preparation and Electrochemical Measurements. HER and OER Tests: All electrochemical measurements were conducted on a CHI 660E electrochemical workstation with a standard three-electrode set-up using the as-synthesized materials as the working electrode, saturated calomel electrode (SCE) as the reference electrode and Pt as the counter electrode in 1 M aqueous KOH. The working electrode was prepared by mixing 5 mg of active material with 0.95 mL ethanol and 0.05 mL Nafion 117 solution (5 wt%). The mixture was sonicated for 30 min and ≈ 0.7 mg of active material was loaded on nickel foam (0.3 cm^2). LSV was recorded at a scan rate of 5 mV s^{-1} to obtain the polarization curves and Tafel plots. Chronoamperometric $i-t$ profile data were collected for 80 h under constant overpotential. LSV data were collected in range of -1.6 to -1.0 V and 0 – 0.8 V to get HER and OER polarization curves, respectively. EIS tests were performed with a frequency loop from 100 kHz to 0.01 Hz by applying a sine wave with an amplitude of 5 mV at open circuit potential. Before HER and OER tests, each working electrode was cycled 50 times at 50 mV s^{-1} until getting a reproducible CV. Conversion

of SCE potential to RHE potentials was done according to the following equation: $E(\text{RHE}) = E(\text{SCE}) + 0.2412 + 0.05916 \times \text{pH}$.

Supporting Information

Supporting Information is available from the Wiley Online Library or from the author.

Acknowledgements

This research was supported by the National Research Foundation (NRF), under Energy Innovation Research Programme (EIRP)R-263-000-B82-279, managed on behalf of Building and Construction Authority (BCA).

Conflict of Interest

The authors declare no conflict of interest.

Keywords

electrocatalysis, functional defects, metal-organic coordinated frameworks, nanoframes

Received: July 25, 2017
Revised: September 11, 2017
Published online: November 8, 2017

- [1] a) Y. Wu, D. Wang, G. Zhou, R. Yu, C. Chen, Y. Li, *J. Am. Chem. Soc.* **2014**, *136*, 11594; b) J. Xu, J. Cui, C. Guo, Z. Zhao, R. Jiang, S. Xu, Z. Zhuang, Y. Huang, L. Wang, Y. Li, *Angew. Chem., Int. Ed.* **2016**, *55*, 6502; c) S. Luo, M. Tang, P. K. Shen, S. Ye, *Adv. Mater.* **2017**, *29*, 1601687.
- [2] a) C. H. Kuo, M. H. Huang, *J. Am. Chem. Soc.* **2008**, *130*, 12815; b) D. Kim, J. Park, K. An, N.-K. Yang, J. G. Park, T. Hyeon, *J. Am. Chem. Soc.* **2007**, *129*, 5812; c) S. Xie, N. Lu, Z. Xie, J. Wang, M. J. Kim, Y. Xia, *Angew. Chem., Int. Ed.* **2012**, *51*, 10266; d) N. Moghimi, M. Abdellah, J. P. Thomas, M. Mohapatra, K. Leung, *J. Am. Chem. Soc.* **2013**, *135*, 10958; e) X. Sun, J. Kim, K. D. Gilroy, J. Liu, T. A. König, D. Qin, *ACS Nano* **2016**, *10*, 8019; f) G. Yilmaz, K. M. Yam, C. Zhang, H. J. Fan, G. W. Ho, *Adv. Mater.* **2017**, *29*, 1606814.
- [3] a) J. Yang, C. Yu, X. Fan, S. Liang, S. Li, H. Huang, Z. Ling, C. Hao, J. Qiu, *Energy Environ. Sci.* **2016**, *9*, 1299; b) M. Behrens, F. Studt, I. Kasatkin, S. Kühn, M. Hävecker, F. Abild-Pedersen, S. Zander, F. Girgsdies, P. Kurr, B. L. Kniep, *Science* **2012**, *336*, 893.
- [4] a) J. Hong, Z. Hu, M. Probert, K. Li, D. Lv, X. Yang, L. Gu, N. Mao, Q. Feng, L. Xie, J. Zhang, D. Wu, Z. Zhang, C. Jin, W. Ji, X. Zhang, J. Yuan, S. Zhang, *Nat. Commun.* **2015**, *6*, 6293; b) W. Zhou, X. Zou, S. Najmaei, Z. Liu, Y. Shi, J. Kong, J. Lou, P. M. Ajayan, B. I. Yakobson, J. C. Idrobo, *Nano Lett.* **2013**, *13*, 2615.
- [5] a) H. Cölfen, S. Mann, *Angew. Chem., Int. Ed.* **2003**, *42*, 2350; b) N. Jongen, P. Bowen, J. Lemaître, J.-C. Valmalette, H. Hofmann, *J. Colloid Interface Sci.* **2000**, *226*, 189; c) T. Wang, H. Cölfen, M. Antonietti, *J. Am. Chem. Soc.* **2005**, *127*, 3246.
- [6] a) P. Nie, L. Shen, H. Luo, B. Ding, G. Xu, J. Wang, X. Zhang, *J. Mater. Chem. A* **2014**, *2*, 5852; b) D. Aguilà, Y. Prado,

- E. S. Koumoussi, C. Mathonière, R. Clérac, *Chem. Soc. Rev.* **2016**, *45*, 203.
- [7] M. Hu, S. Ishihara, K. Ariga, M. Imura, Y. Yamauchi, *Chem. - Eur. J.* **2013**, *19*, 1882.
- [8] M. Hu, S. Furukawa, R. Ohtani, H. Sukegawa, Y. Nemoto, J. Reboul, S. Kitagawa, Y. Yamauchi, *Angew. Chem.* **2012**, *124*, 1008.
- [9] S. Pintado, S. Goberna-Ferrón, E. C. Escudero-Adán, J. R. Galán-Mascarós, *J. Am. Chem. Soc.* **2013**, *135*, 13270.
- [10] a) R. Q. Song, H. Cölfen, *Adv. Mater.* **2010**, *22*, 1301; b) X. J. Zheng, Q. Kuang, T. Xu, Z. Y. Jiang, S. H. Zhang, Z. X. Xie, R. B. Huang, L. S. Zheng, *J. Phys. Chem. C* **2007**, *111*, 4499; c) M. Hu, J. S. Jiang, R.-P. Ji, Y. Zeng, *CrystEngComm* **2009**, *11*, 2257; d) X. Roy, L. K. Thompson, N. Coombs, M. J. MacLachlan, *Angew. Chem., Int. Ed.* **2008**, *47*, 511.
- [11] a) W. Zhang, Y. Zhao, V. Malgras, Q. Ji, D. Jiang, R. Qi, K. Ariga, Y. Yamauchi, J. Liu, J. S. Jiang, *Angew. Chem.* **2016**, *128*, 8368; b) E. Uchaker, G. Cao, *Nano Today* **2014**, *9*, 499.
- [12] N. Tian, Z. Y. Zhou, S. G. Sun, Y. Ding, Z. L. Wang, *Science* **2007**, *316*, 732.
- [13] Q. Chen, Y. Jia, S. Xie, Z. Xie, *Chem. Soc. Rev.* **2016**, *45*, 3207.
- [14] a) X. Yu, Z. Sun, Z. Yan, B. Xiang, X. Liu, P. Du, *J. Mater. Chem. A* **2014**, *2*, 20823; b) C. Xia, Q. Jiang, C. Zhao, M. N. Hedhili, H. N. Alshareef, *Adv. Mater.* **2016**, *28*, 77; c) J. P. Perdew, J. A. Chevary, S. H. Vosko, K. A. Jackson, M. R. Pederson, D. J. Singh, C. Fiolhais, *Phys. Rev. B* **1992**, *46*, 6671; d) P. L. Gai, M. A. Harmer, *Nano Lett.* **2002**, *2*, 771.
- [15] a) L. H. Jones, B. I. Swanson, *Acc. Chem. Res.* **1976**, *9*, 128; b) W. P. Griffith, *Q. Rev., Chem. Soc.* **1962**, *16*, 188.
- [16] a) G. Somorjai, D. Blakely, *Nature* **1975**, *258*, 580; b) C. Wang, Z. Zhang, G. Yang, Q. Chen, Y. Yin, M. Jin, *Nano Lett.* **2016**, *16*, 5669; c) J. Maier, *Angew. Chem., Int. Ed.* **1993**, *32*, 313; d) J. Maier, *Angew. Chem., Int. Ed.* **1993**, *32*, 528; e) S. He, C. Li, H. Chen, D. Su, B. Zhang, X. Cao, B. Wang, M. Wei, D. G. Evans, X. Duan, *Chem. Mater.* **2013**, *25*, 1040.
- [17] a) X. Long, G. Li, Z. Wang, H. Zhu, T. Zhang, S. Xiao, W. Guo, S. Yang, *J. Am. Chem. Soc.* **2015**, *137*, 11900; b) D. Y. Wang, M. Gong, H. L. Chou, C. J. Pan, H. A. Chen, Y. Wu, M. C. Lin, M. Guan, J. Yang, C. W. Chen, *J. Am. Chem. Soc.* **2015**, *137*, 1587.
- [18] C. Xiao, X. Lu, C. Zhao, *Chem. Commun.* **2014**, *50*, 10122.